

Article

Spatial Gap-Filling of GK2A Daily Sea Surface Temperature (SST) around the Korean Peninsula Using Meteorological Data and Regression Residual Kriging (RRK)

Jihye Ahn ¹ and Yangwon Lee ^{2,*}¹ Research Institute for Geomatics, Pukyong National University, Busan 48513, Korea² Department of Spatial Information Engineering, Division of Earth Environmental System Science, Pukyong National University, Busan 48513, Korea

* Correspondence: modconfi@pknu.ac.kr

Abstract: Satellite remote sensing can measure large ocean surface areas, but the infrared-based sea surface temperature (SST) might not be correctly calculated for the pixels under clouds, resulting in missing values in satellite images. Early studies for the gap-free raster maps of satellite SST were based on spatial interpolation using in situ measurements. In this paper, however, an alternative spatial gap-filling method using regression residual kriging (RRK) for the Geostationary Korea Multi-Purpose Satellite-2A (GK2A) daily SST was examined for the seas around the Korean Peninsula. Extreme outliers were first removed from the in situ measurements and the GK2A daily SST images using multi-step statistical procedures. For the pixels on the in situ measurements after the quality control, a multiple linear regression (MLR) model was built using the selected meteorological variables such as daily SST climatology value, specific humidity, and maximum wind speed. The irregular point residuals from the MLR model were transformed into a residual grid by optimized kriging for the residual compensation for the MLR estimation of the null pixels. The RRK residual compensation method improved accuracy considerably compared with the in situ measurements. The gap-filled 18,876 pixels showed the mean bias error (MBE) of -0.001 °C, the mean absolute error (MAE) of 0.315 °C, the root mean square error (RMSE) of 0.550 °C, and the correlation coefficient (CC) of 0.994 . The case studies made sure that the gap-filled SST with RRK had very similar values to the in situ measurements to those of the MLR-only method. This was more apparent in the typhoon case: our RRK result was also stable under the influence of typhoons because it can cope with the abrupt changes in marine meteorology.

Keywords: Geostationary Korea Multi-Purpose Satellite-2A (GK2A); sea surface temperature (SST); regression residual kriging (RRK); spatial gap-filling

Citation: Ahn, J.; Lee, Y. Spatial Gap-Filling of GK2A Daily Sea Surface Temperature (SST) around the Korean Peninsula Using Meteorological Data and Regression Residual Kriging (RRK). *Remote Sens.* **2022**, *14*, 5265. <https://doi.org/10.3390/rs14205265>

Academic Editors: Jorge Vazquez and Eileen Maturi

Received: 10 September 2022

Accepted: 19 October 2022

Published: 21 October 2022

Publisher's Note: MDPI stays neutral with regard to jurisdictional claims in published maps and institutional affiliations.



Copyright: © 2022 by the authors. Licensee MDPI, Basel, Switzerland. This article is an open access article distributed under the terms and conditions of the Creative Commons Attribution (CC BY) license (<https://creativecommons.org/licenses/by/4.0/>).

1. Introduction

Sea surface temperature (SST) is a crucial variable for the atmosphere–ocean interaction and plays a vital role in exchanging heat, momentum, and moisture between the atmosphere and the ocean. Because SST data are used in climate modeling, global heat balance, weather forecasting, and marine ecosystem monitoring [1–3], many efforts have been made for spatially continuous SST data with higher accuracy [4].

The accuracy of in situ SST observations from ships, drifting buoys, moorings, and Argo floats is quite reliable, but they are point-based measurements sparsely distributed in space [4]. On the other hand, satellite remote sensing can measure large ocean surface areas using infrared sensors [5]. However, the infrared-based SST might not be correctly calculated for the pixels under clouds, aerosols, and dust, resulting in missing values in satellite images [6–9]. Although microwave sensors have the advantage of penetrating through clouds, the coarse spatial resolution over 10 km is not appropriate for regional-

scale studies. Alternatively, spatial gap-filling for the infrared SST products at a spatial resolution of 1 or 2 km can be more effective for examining local-scale changes at various intervals of the day, month, season, and year [5].

Early studies for the gap-free raster maps of satellite SST were based on spatial interpolation using in situ measurements and National Oceanic and Atmospheric Administration (NOAA) SST [10]. Various types of kriging could help a faster interpolation for gap-filling of moderate resolution imaging spectroradiometer (MODIS) SST [11]. Further, a reconstruction process using empirical orthogonal function (EOF) and the advanced very high-resolution radiometer (AVHRR) SST was developed due to its feasibility, not requiring priori knowledge for correlation functions [12–14]. However, these reconstruction methods had limited accuracy for the sparse data along the coasts due to the mixed pixel problem and coarse resolution of the satellite data. To overcome this, a hybrid method combining EOF and kriging was proposed for a more realistic gap-filling of AVHRR and MODIS SST [15]. This hybrid method can effectively make up the EOF-only method by coping with sparse data. More recent studies presented an artificial neural network (ANN) approach [16] based on the non-linear relationships between SST and marine meteorology variables, which is an initial stage for the spatial gap-filling of SST products.

The residual is the difference between a true and a modeled value and inevitably occurs in statistical models such as kriging, EOF, and ANN. It is simply calculated as actual minus predicted value. The mean absolute error (MAE) or root mean square error (RMSE) may be a proxy measure of the residual, and the previous studies showed the RMSE between 0.680 °C and 0.950 °C [11–13,15]. The residuals are the shortage of a model against in situ observations and indicate the uncertainties that should be reduced to improve the reliability of a model. Regression residual kriging (RRK) is a method to enhance the model accuracy by the compensation of the residual based on the spatial autocorrelation in the residuals [17]. For the residual compensation, RRK creates a continuous residual surface from the point residuals remaining after the estimation model. The residual compensation is conducted by adding a residual surface to an estimated raster, which produces a corrected result and improved accuracy [18]. Previous studies based on RRK have been carried out for the spatial gap-filling of the raster data and the spatial interpolation of the point measurements, such as soil properties and air pollution [17,19–24]. The RRK was used to improve the estimation of forest stock volume from Landsat 8 and Sentinel-2 images and produced a more accurate result ($\text{RMSE} = 49.68 \text{ m}^3 \text{ ha}^{-1}$) than Multiple Linear Regression (MLR) ($\text{RMSE} = 57.39 \text{ m}^3 \text{ ha}^{-1}$) [17]. The case of mapping nitrogen dioxide (NO_2) concentrations using RRK [19] showed a normalized RMSE of 0.94%, a relatively lower error than MLR (0.95%). In a soil moisture gap-filling study [21], the RMSE of RRK was 6.7%, whereas that of MLR was 7.0%. An experiment for soil reaction (pH) mapping [24] showed that RRK was more precise than the ordinary kriging (OK) by 1.81%.

Meanwhile, recent advances in satellite remote sensing have enabled multiple geostationary satellites worldwide, covering America, Europe, and Asia. The Geostationary Korea Multi-Purpose Satellite-2A (GK2A) was launched on 5 December 2018, and has been providing various meteorological products, including SST, at intervals of 10 min on a 2 km grid [25]. However, a spatial gap-filling method to create continuous raster data is not established yet. The objective of this study was to develop a spatial gap-filling framework for GK2A daily SST using RRK for the seas around the Korean Peninsula. It is the first challenge for the SST from geostationary satellites that can minimize the uncertainty of the SST estimate using RRK by residual compensation. For quality control, extreme outliers were removed from the in situ measurements and the satellite images for SST by using statistical procedures. Then, a regression model was built for the valid SST pixels using multiple meteorological variables. The irregular point residuals from the regression model were converted into a raster surface by optimized kriging for use in the residual compensation. The regression estimates calculated for the invalid SST pixels were then corrected by the residual compensation. The accuracy statistics of the proposed gap-filling

method by RRK were presented to show the performance of our approach for the high-quality gap-free raster map of daily SST.

2. Study Area

The study area is around the Korean Peninsula between 30.5°N to 40.5°N and 122.5°E to 132.5°E. Figure 1a shows a map of East Asia including the study area. Figure 1b shows the locations of the 137 in situ SST measurements by the Korea Meteorological Administration (KMA) and the Korea Hydrographic and Oceanographic Agency (KHOA) used for the reference data. Green points are the locations of 82 KMA stations, and red points denote the locations of KHOA stations. They are used as reference data for the validation of GK2A SST gap-filling. Figure 1c shows the locations of nine stations used for the performance evaluation, particularly for the far seas more than 30 km from the coastline (Ongjinsocheongcho, Incheon, Seohae 170, Seohae 206, Sinangageocho, Ulsan, Pohang, Uljin, and Donghae).

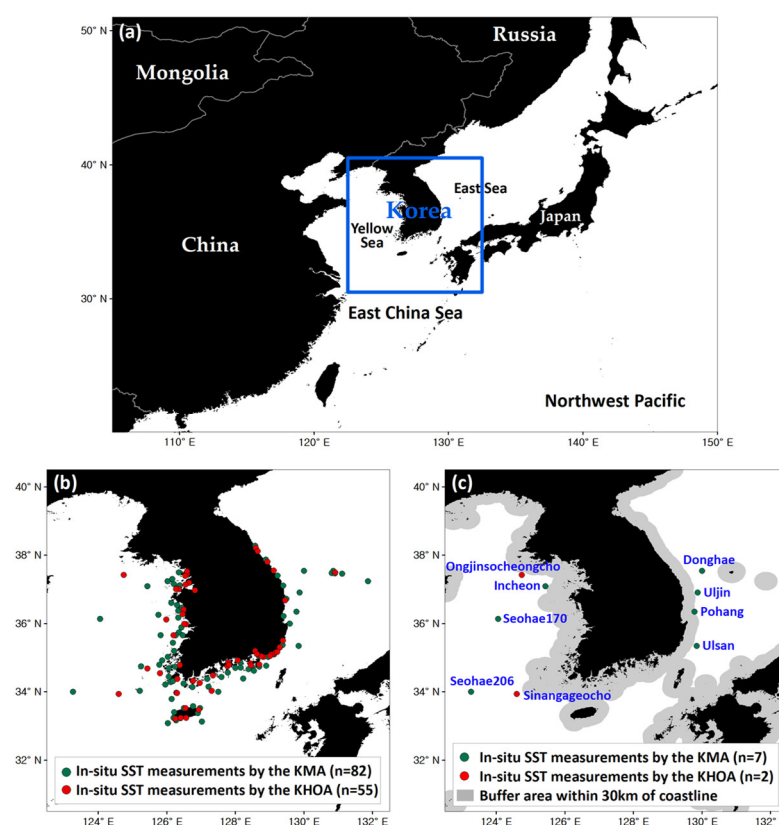


Figure 1. (a) A map of East Asia including Korean Peninsula, where the blue rectangle indicates the study area (30.5–40.5°N and 122.5–132.5°E); (b) 137 stations for in situ SST measurements by the Korea Meteorological Administration (KMA) and the Korea Hydrographic and Oceanographic Agency (KHOA) used as reference data for the validation of GK2A SST gap-filling and (c) nine stations for the performance evaluation, particularly for the far seas outside 30 km from the coastline.

3. Data

Table 1 summarizes the data used in our experiment between 1 January and 31 December 2020. The SST regression model for spatial gap-filling includes GK2A SST for a target variable and the local data assimilation and prediction system (LDAPS) data, and the operational sea surface temperature and ice analysis (OSTIA) climatology value as explanatory variables. The in situ SST measurements were used for accuracy validation.

Table 1. Summary of the data used in this study.

Data	Use	Spatial resolution	Temporal resolution	Aggregation Method
GK2A SST	Target variable	2 km	Daily	Daily product itself
LDAPS	Explanatory variables	1.5 km	3 h	Daily average of 3-h data
OSTIA SST	Explanatory variables	0.05°	Daily	Mean of 14-year data for every day
In situ SST Validation reference		Point	1 h	Daily average of 1-h data

3.1. GK2A SST

GK2A with an advanced meteorological imager (AMI) shows better performance than its predecessor, the Communication, Ocean, and Meteorological Satellite (COMS) with a meteorological imager (MI) [26]. It has 16 spectral bands with a spatial resolution of approximately 2 km and the temporal resolution of 10 min (Table 2).

Table 2. GK2A channel information including the center of wavelength, bandwidth, and spatial resolution.

Category	Channel No.	Center of Wavelength (μm)	Bandwidth (μm)	Resolution (km)
Visible	1	0.47	0.43–0.48	1
	2	0.51	0.50–0.52	1
	3	0.64	0.63–0.66	0.5
Near Infrared	4	0.86	0.85–0.87	1
	5	1.37	1.37–1.38	2
	6	1.61	1.60–1.62	2
Water Vapor	7	3.83	3.74–3.96	2
	8	6.20	6.06–6.42	2
	9	6.90	6.89–7.01	2
Infrared	10	7.30	7.26–7.43	2
	11	8.60	8.44–8.76	2
	12	9.60	9.54–9.72	2
	13	10.40	10.25–10.61	2
	14	11.20	11.08–11.32	2
	15	12.30	12.15–12.45	2
	16	13.30	13.21–13.39	2

The GK2A level 3 daily SST product is provided by National Meteorological Satellite Center (NMSC) [27] since July 2019. A multi-band SST algorithm was employed to retrieve SST using the brightness temperature of four thermal infrared bands (8.6, 10.5, 11.2, and 12.3 μm) and several empirical coefficients [28], as expressed in Equation (1):

$$SST = C_1 T_{10.5} + C_2 (T_{10.5} - T_{12.3}) + \{C_3 (T_{10.5} - T_{8.6}) + C_4 (T_{10.5} - T_{11.2})\} (\sec \theta - 1) + \{C_5 (T_{10.5} - T_{8.6}) + C_6 (T_{10.5} - T_{11.2}) + C_7 (T_{10.5} - T_{12.3})\} T_{FG} + C_8 \quad (1)$$

where C_* is the empirical coefficient derived by using in situ measurements; θ is the viewing zenith angle; T_{FG} is the first guess SST; $T_{8.6}$, $T_{10.5}$, $T_{11.2}$, and $T_{12.3}$ are the brightness temperature of each wavelength. This algorithm can be applied to both day and night and minimize the possible day–night discontinuities [29]. The daily SST data between 1 January and 31 December, 2020 was used for our experiment.

3.2. LDAPS Data

LDAPS data were used as explanatory variables of our spatial gap-filling model for the invalid pixels of the GK2A daily SST product. LDAPS is based on the unified model (UM) designed by the United Kingdom (UK) Met Office. LDAPS produces a local-scale forecast and reanalysis around the Korean Peninsula and helps overcome the spatial resolution and time-scale limitations of the global and regional models. The data is provided eight times (00, 03, 06, 09, 12, 15, 18, and 21 UTC) per day on a 1.5 km grid for the 70 vertical levels up to 40 km [30] based on a three-dimensional variational (3DVAR) data assimilation technique [31] (Figure 2). Table 3 shows the candidates for the explanatory variables from LDAPS for our SST gap-filling: specific humidity, air temperature, skin temperature, relative humidity, maximum wind speed, and precipitation. The eight-times data were aggregated as daily averages to match the GK2A daily SST.

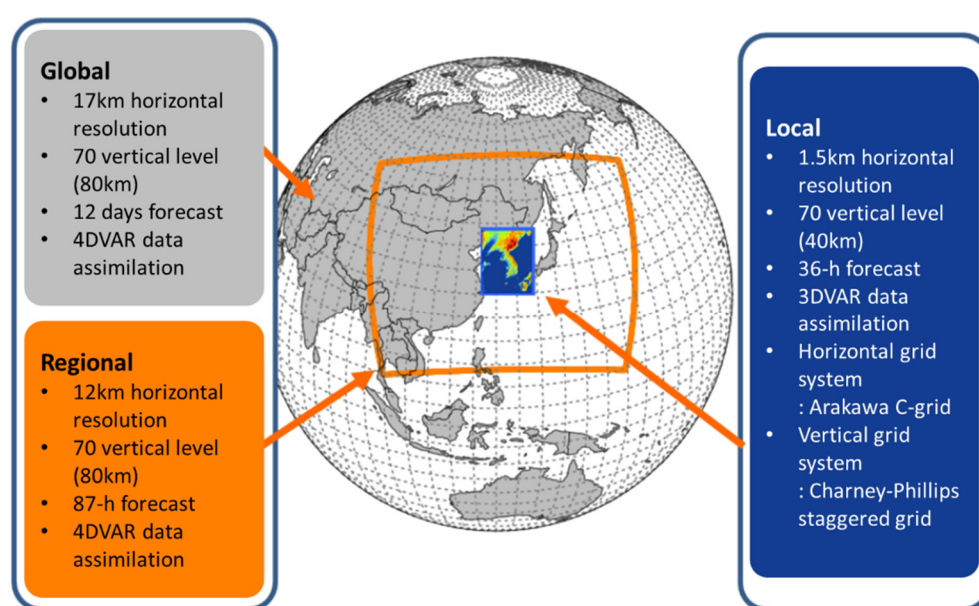


Figure 2. Summary of the global, regional, and local forecasting models by KMA.

Table 3. Candidate explanatory variables from LDAPS for the spatial gap-filling of GK2A daily SST.

Abbreviation	Description	Units
SH	Specific humidity 1.5 m above ground	kg/kg
AT	Air temperature 1.5 m above ground	K
ST	The temperature at the ground or water surface	K
RH	Relative humidity 1.5 m above ground	%
MWS	Maximum wind speed (1-h maximum) 0 m above ground	m/s
PR	1-h average precipitation at ground or water surface	kg/m ² /s

3.3. OSTIA SST Climatology Data

The daily value of OSTIA SST was aggregated for 14 years (2007 to 2020). This was used as an additional explanatory variable to reflect the long-term SST trend for spatial gap-filling. OSTIA SST is a globally gridded gap-filled 0.05° data provided by UK Met Office since 2007 [32]. We aggregated the daily SST for 14 years to create daily climatology data for the Korean Peninsula.

3.4. In Situ SST Measurements

We prepared the validation reference for our spatial gap-filling model from the in situ SST measurements by KMA and KHOA. The hourly data was observed from the ocean meteorological buoys at a depth of 0.6 m and 0.3 m [33] and the ocean wave buoys that monitor local wave heights at a depth of about 0.3 m [33,34]. The hourly in situ measurements provided by KMA and KHOA were aggregated to the daily average to match GK2A daily SST.

4. Methods

4.1. Overview

Figure 3 shows the proposed spatial gap-filling method consisting of pre-processing, MLR modeling, RRK modeling, and accuracy validation. The preprocessing for the GK2A SST images includes coordinate reference system (CRS) transformation, land/sea masking, and outlier removal. In the MLR modeling step, we selected appropriate explanatory variables by considering the correlation with GK2A SST and a multicollinearity test. An MLR model was built using the dataset on the in situ measurement points and then applied to the null pixels to get the estimates. In the RRK modeling step, the irregular MLR residual pixels were converted to a continuous surface by optimized kriging. The residual raster was added to the MLR estimate raster for the residual compensation to produce a gap-free SST map. Finally, the accuracy validation with the in situ SST was conducted to evaluate the gap-free raster maps of the GK2A daily SST.

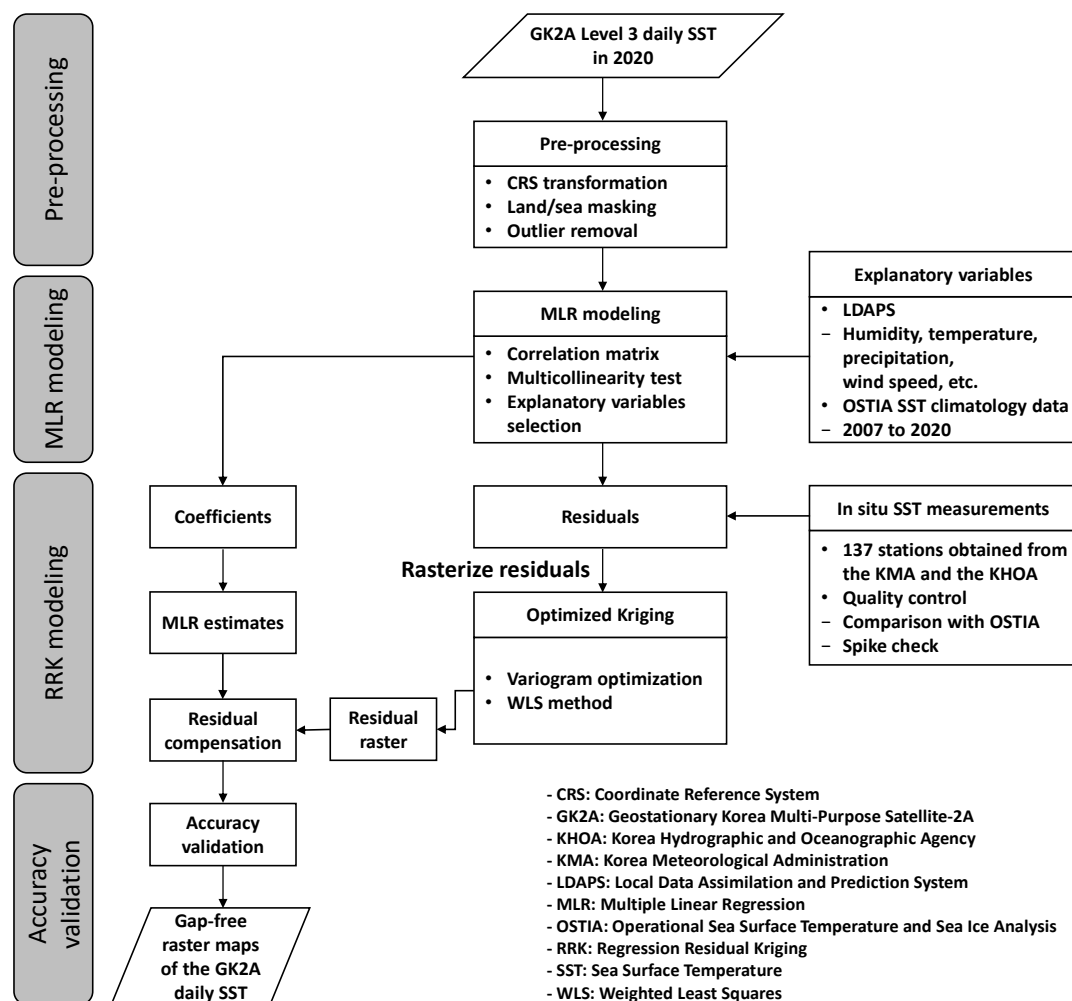


Figure 3. Flow chart of the spatial gap-filling method proposed in this study.

4.2. Quality Control of In Situ Measurements

Measurement errors of buoys are due to various causes, such as strong tides, structural turbulence, adhesion of marine species, and defects in observation sensors. Outliers generally refer to the data that exists in a small proportion of the entire dataset and have very exceptional values compared with the other data. In this study, if the measurement error of the in situ SST was found by quality control (QC), it was regarded as an outlier to be removed. We performed QC for the in situ SST using two statistical techniques and procedures. First, the daily OSTIA SST with high accuracy around the Korean Peninsula [35–37] was compared with the in situ SST. For the entire time series of 366 days at each station, the standard derivation of the difference between the in situ SST and the OSTIA values was calculated as ($\sigma(diff)$). If the difference ($|in_situ - OSTIA|$) between the in situ SST (in_situ) and the OSTIA values ($OSTIA$) exceeded the $12\sigma(diff)$, it was considered an outlier and removed from the dataset. Next, a spike test recommended by Integrated Ocean Observing System (IOOS) was performed [38]. The annual standard deviation of the in situ SST for each station was calculated as ($\sigma(obs1year)$). If the difference ($|in_situ - neighbors|$) between the in situ SST (in_situ) and the mean of ± 7 days' values ($neighbors$) exceeds $\sigma(obs1year)$, it was considered an outlier. Out of 48,151 observations from 137 stations, 20 cases from 14 stations (0.04%) were removed as outliers (Table 4). Indeed, the outliers are dependent on the threshold value of the outlier detection algorithm. In this experiment, we set a somewhat strict threshold value so that relatively few outliers were found. Even though the number of outliers was not many, they should be detected and removed because they had seriously inappropriate values compared with neighboring values. Figure 4 shows a time series of the daily SST at the Seocheon and Udo stations as an example of the outlier detection.

Table 4. Overview of in situ SST observations. A total of 20 cases from 14 stations were removed as outliers, and 48,131 observations from 137 stations were finally used.

Organiza- tion	Data Name	Temporal Resolu- tion	Outlier Removal		Finally Used Data	
			No. of Stations	No. of Data	No. of Stations	No. of Data
KMA	Ocean meteorological buoy	1 h	1	1	21	7486
	Ocean wave buoy	1 h	8	9	61	21,381
	Tidal station	1 h	2	3	30	10,864
KHOA	Ocean observation buoy	1 h	3	7	23	7762
	Ocean research station	1 h	0	0	2	638
Sum	-	-	14	20	137	48,131

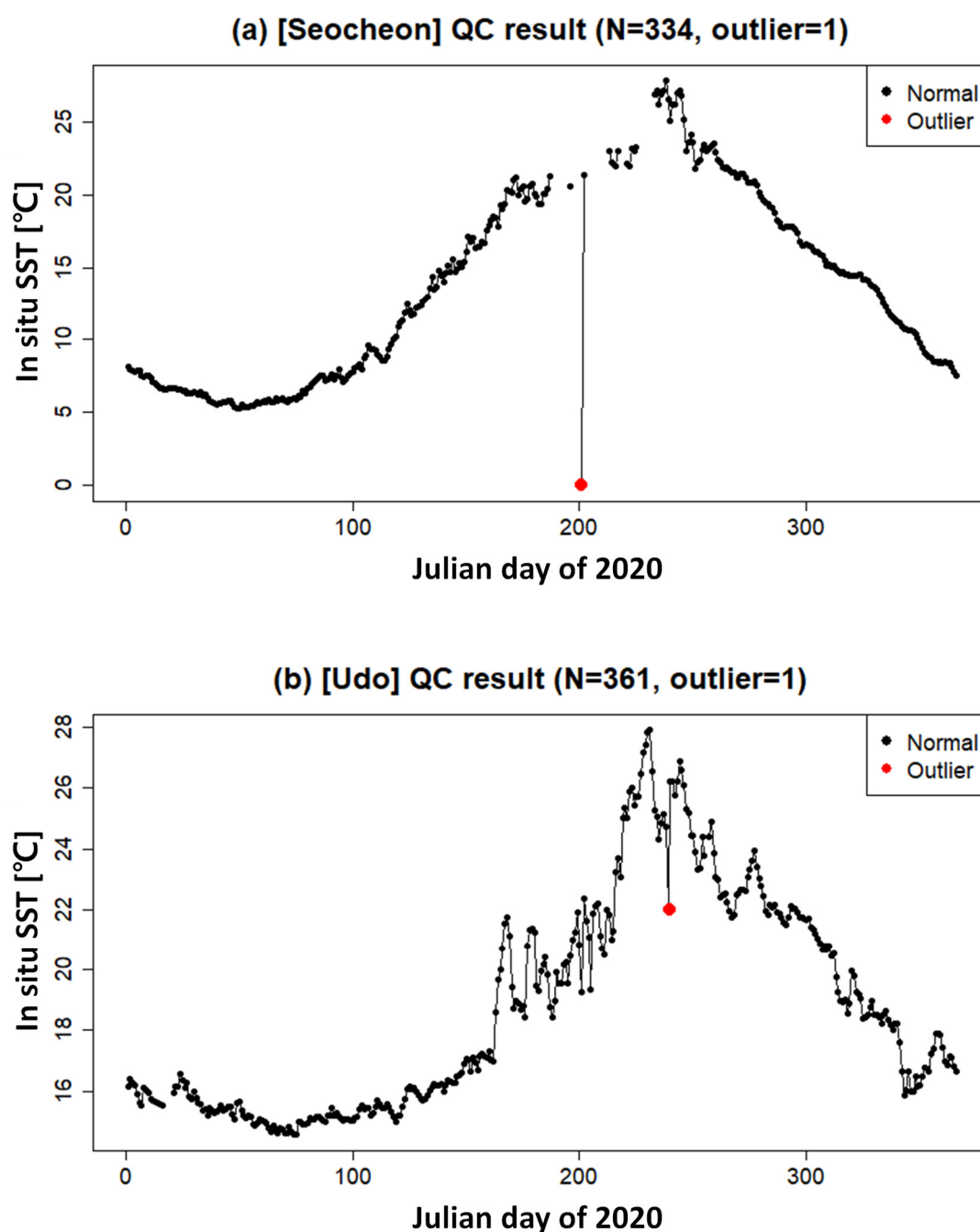


Figure 4. Example of quality control results for in situ SST observations at (a) Seocheon and (b) Udo. The black point denotes the normal data of the time series, and the red point is the outlier detected by the quality control process.

4.3. Pre-Processing of GK2A SST

The CRS of GK2A SST was converted from Lambert conformal conic (LCC) to World Geodetic System 1984 (WGS84) for the CRS unification of all data needed for the matchup database. We distinguished the sea pixel using a land/sea mask created from an electronic navigation chart (ENC) provided by the KHOA. Outlier detection was also conducted for the GK2A SST that may be contaminated by cloud or land pixels [39]. We detected extreme outliers showing very different values from the neighboring pixels [40,41] using the deviation from spatial autocorrelation trend (DSAT) method [42]. Usually, the similarity of

data values increases as the distance of the locations decreases [43]. Such a spatial autocorrelation is found in SST, and an extreme deviation from the spatial autocorrelation trend can be regarded as an outlier for the satellite SST images. Figure 5 shows the logic of the DSAT method. A spatial autocorrelation pattern is expressed by a Moran scatter plot (MSP) that shows the relationship between the z-score of a target pixel and the mean z-score of the neighboring eight pixels [44]. The DSAT for each pixel can be calculated as the deviation from the 1:1 line of the MSP. If the DSAT exceeds a given threshold ($k\sigma(DSAT)$), it is regarded as an outlier pixel. The search radius for calculating the mean z-score of the neighbors was set to 25×25 pixels, considering the spatially homogeneous characteristics of SST. The constant for filtering extreme outliers was set to 12 through many times iterations.

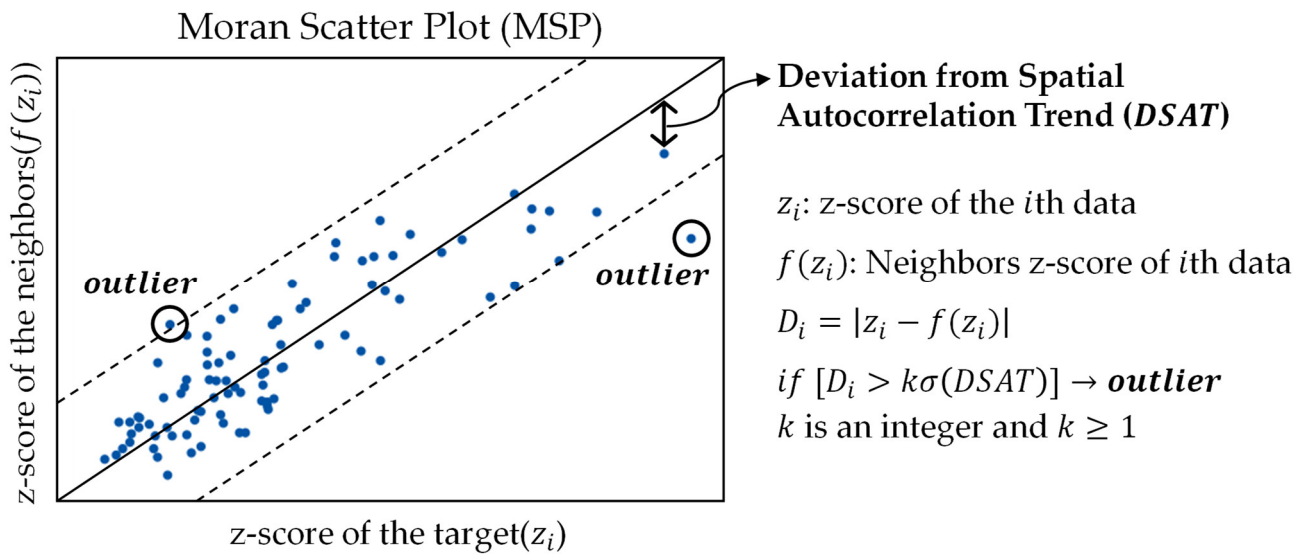


Figure 5. Outlier detection using deviation from the spatial autocorrelation trend (DSAT).

4.4. MLR Modeling

MLR is used to model the relationship between the GK2A SST and meteorological factors. An MLR model having k explanatory variables (x_1, x_2, \dots, x_k) can be expressed as Equation (2).

$$y = \beta_0 + \beta_1 x_1 + \beta_2 x_2 + \dots + \beta_k x_k + \varepsilon \quad (2)$$

where y is a target variable, x_1, x_2, \dots, x_k are k explanatory variables that affect the target variable, $\beta_1, \beta_2, \dots, \beta_k$ are regression coefficients corresponding to each explanatory variable (x_1, x_2, \dots, x_k), β_0 is the intercept and ε is the error term. GK2A SST was set to the target variable, and the meteorological factors from LDAPS and OSTIA data were used as explanatory variables such as specific humidity, air temperature, skin temperature, relative humidity, maximum wind speed, precipitation, and daily SST climatology value. Figure 6 shows the correlation between all candidate explanatory variables including GK2A SST of the 27,099 pixels on the in situ measurement points in 2020. Precipitation and relative humidity were excluded because they had a low correlation with GK2A SST. Temperature variables had a high correlation with GK2A SST, but air and skin temperature were excluded because they could not pass the multicollinearity test with the variance inflation factor (VIF) exceeding 10. Finally, specific humidity, maximum wind speed, and daily SST climatology value were selected as explanatory variables of the MLR model. Figure 7 shows the scatter plot of the relationships between GK2A SST and selected explanatory variables.

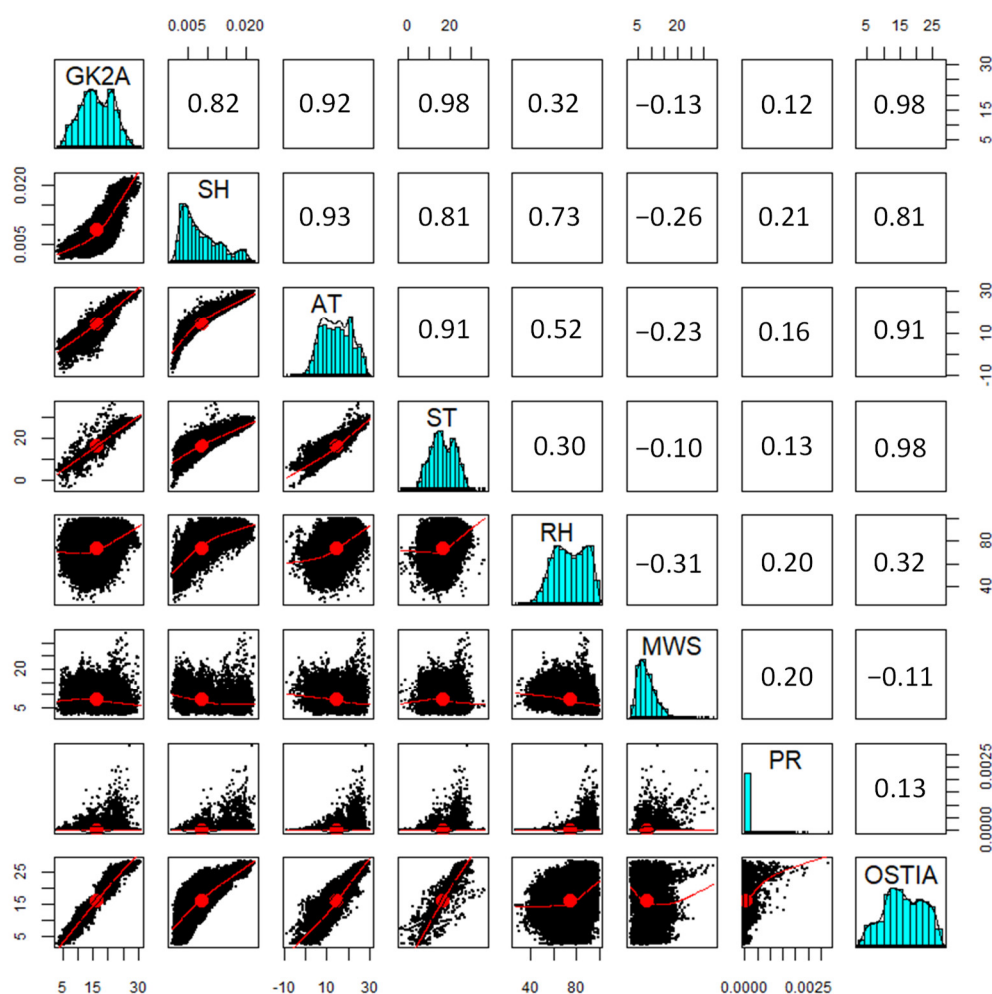
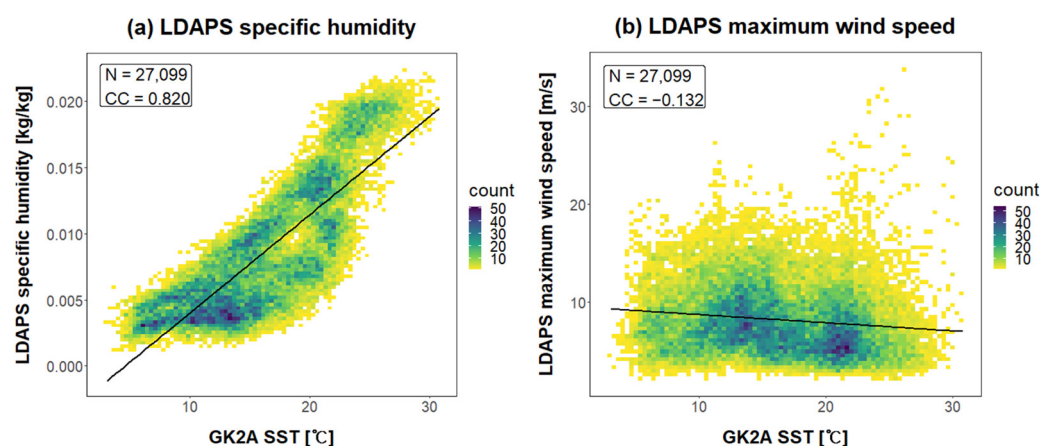


Figure 6. Correlation matrix between variables: bivariate scatter plots below the diagonal, histograms on the diagonal, and the Pearson correlation coefficients above the diagonal. In bivariate scatter plots, the x -axis refers to the variable located at the top of the matrix, and the y -axis refers to the variable located to the right of the matrix. (GK2A = GK2A SST ($^{\circ}$ C), SH = Specific humidity (kg/kg), AT = Air temperature ($^{\circ}$ C), ST = Skin temperature ($^{\circ}$ C), RH = Relative humidity (%), MWS = Maximum wind speed (m/s), PR = Precipitation (kg/m²/s), and OSTIA = OSTIA daily SST climatology value ($^{\circ}$ C)).



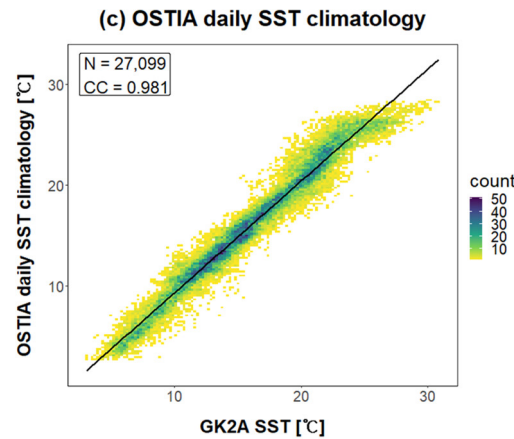


Figure 7. Scatter plot of the relationships between GK2A SST and (a) LDAPS specific humidity, (b) LDAPS maximum wind speed, and (c) OSTIA daily SST climatology value. 27,099 pixels were matched to the in situ measurement points in 2020.

4.5. Regression Residual Kriging

RRK is an estimation model that combines a regression model and the residual compensation using kriging of the regression residuals [18]. RRK consists of four steps: (1) MLR modeling, (2) calculation of point residuals, (3) creation of the residual raster using an optimized kriging, and (4) the residual compensation by adding the residual raster to the MLR estimation raster [17,22]. RRK can be briefly expressed as

$$\hat{z} = \varphi_0 + \sum_{i=1}^n \varphi_i x_i(s) + \sum_{j=1}^m \lambda_j \varepsilon(s_j) \quad (3)$$

where φ_0 and φ_i are the estimated values by regression model, x_i is an explanatory variable that explains target variable variation, n is the number of observations, λ_i is kriging weight, and ε is the kriged model residual at observation locations [17].

Regarding the third step, the MLR residuals on the irregular points were interpolated by the optimized kriging based on the variogram optimization using weighted least squares (WLS) method [45]. This is to find the optimal combination of the variogram parameters such as the variogram model (spherical, exponential, Gaussian, Matern, and Steins), range, sill, and nugget through iterative simulations to minimize the difference between an experimental and a theoretical variogram [46] (Figure 8). Figure 9 shows the RRK process for spatial gap-filling with the example of 10 April 2020. (a) and (b) denote SST images before spatial gap-filling and after MLR modeling. (c) is point residuals for each measurement station and (d) shows the raster residual surface created by the optimized kriging using WLS method. (e) is a gap-free SST map produced by the residual compensation.

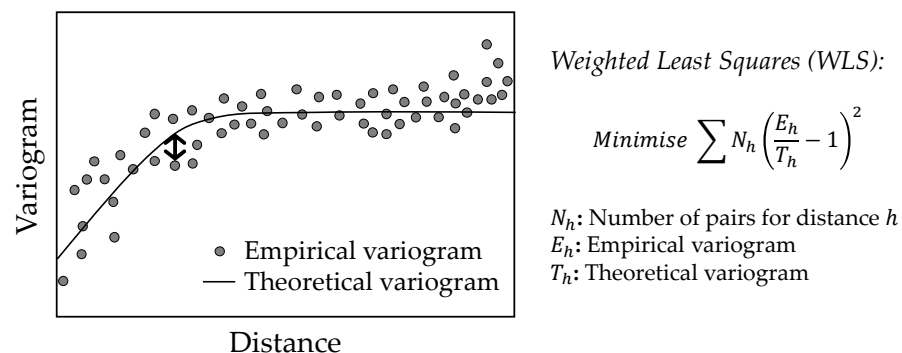


Figure 8. Variogram optimization using the weighted least squares (WLS) of the dissimilarity of the empirical and theoretical variograms.

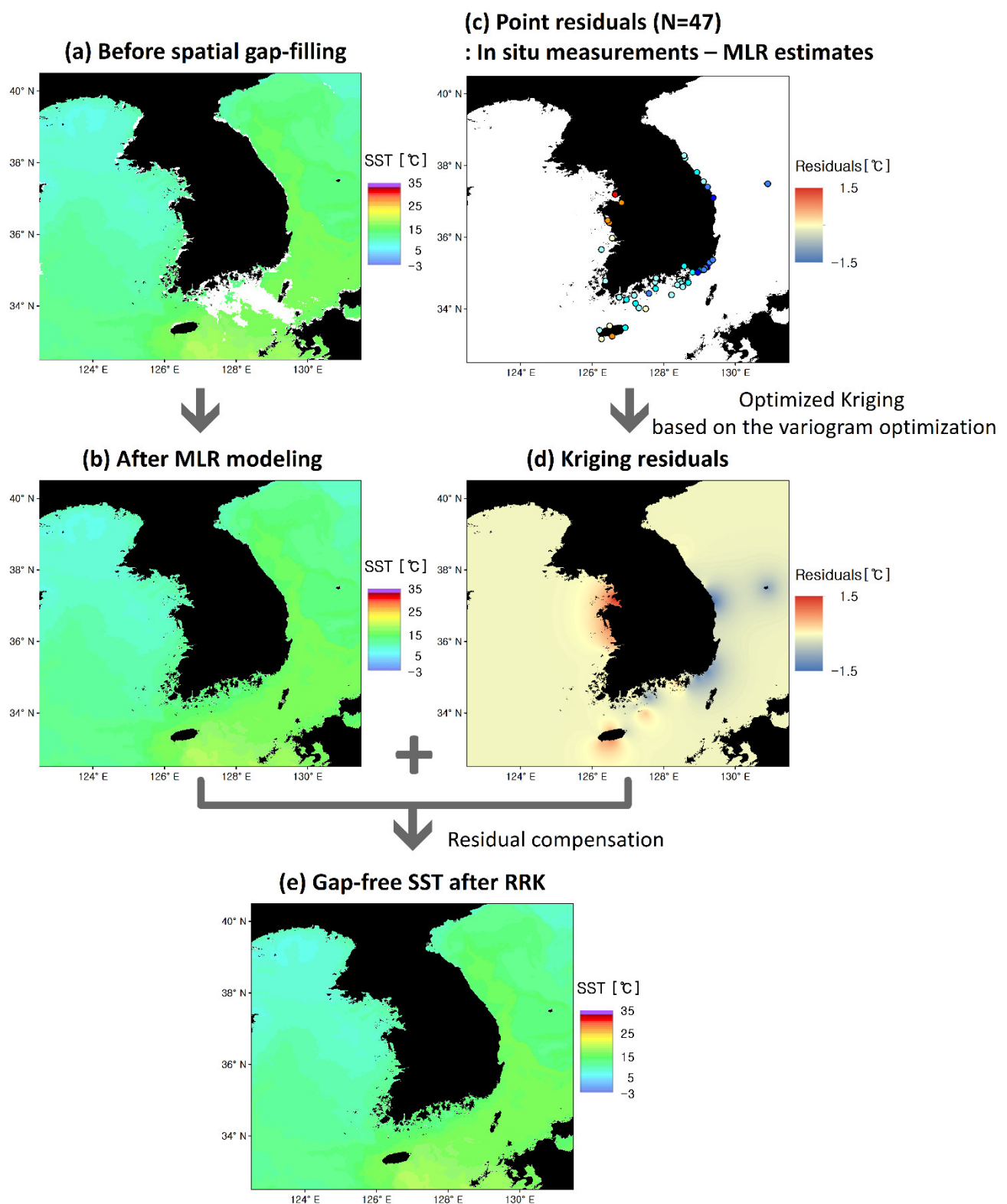


Figure 9. RRK process with the example of 10 April 2020. (a,b) denote images before spatial gap-filling and after MLR modeling, respectively. (c) point residuals, (d) kriging residuals, and (e) gap-free SST after RRK.

4.6. Accuracy Evaluation

Accuracy evaluation for the gap-free raster maps of the GK2A daily SST was conducted using the in situ SST. Four common statistical indices were used to quantify the accuracy: Mean Bias Error (MBE), MAE, RMSE, and Correlation Coefficient (CC).

$$MBE = \frac{1}{n} \sum_{i=1}^n (x_i - y_i) \quad (4)$$

$$MAE = \frac{1}{n} \sum_{i=1}^n |x_i - y_i| \quad (5)$$

$$RMSE = \sqrt{\frac{1}{n} \sum_{i=1}^n (x_i - y_i)^2} \quad (6)$$

$$CC = \frac{\sum_{i=1}^n (x_i - \bar{x})(y_i - \bar{y})}{(n-1)s_x s_y} \quad (7)$$

where x refers to SST estimates, y refers to in situ measurements, \bar{x} and \bar{y} are the means of x and y , respectively. s_x and s_y refer to the standard deviations of x and y , and n refers to number of the data. Positive MBE represents an overestimation whereas negative MBE indicates an underestimation of the model prediction. MAE measures the mean of the absolute magnitude of the errors in the estimation. RMSE, a quadratic measure for the average size of the error, is useful when evaluating relatively large errors. The CC indicates the correlation between in situ measurements and model estimates: 1(−1) indicates an extremely positive (negative) relationship between two data.

5. Results and Discussion

5.1. Removal of Outlier Pixels

As a result of the outlier detection using DSAT for the 366 images of GK2A daily SST product in 2020, 3668 outlier pixels (0.007%) were detected out of a total of 52,400,000 pixels. Figure 10 shows the scatter plots for the in situ and the GK2A SST before and after the outlier removal using DSAT. The MBE, MAE, and RMSE were quite decreased, and CC was slightly increased after the outlier removal, indicating the effectiveness of the outlier detection technique using DSAT.

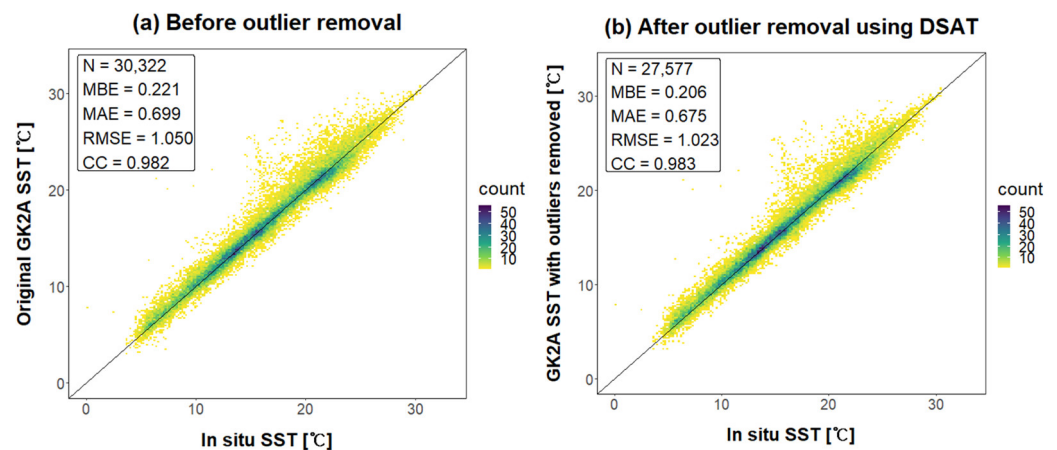


Figure 10. Scatter plots for the in situ and the GK2A SST (a) before outlier removal and (b) after outlier removal using DSAT.

Figure 11 shows the example SST maps before and after outlier detection on 1 June 2020. The color bars for SST in this paper are officially used by KMA. The annual minimum SST of the sea area around the Korean Peninsula is approximately $-3\text{ }^{\circ}\text{C}$, and the maximum SST is approximately $32\text{ }^{\circ}\text{C}$. So, $35\text{ }^{\circ}\text{C}$ is an extremely high temperature for the study area, and purple was used to distinguish it from the other pixels. Outlier pixels colored in black had quite different values from the neighbor pixels (Figure 11b,d). Most of the outlier pixels were found near the coastline. Because GK2A has a spatial resolution of 2 km, some pixels may have slightly contaminated radiance values, particularly around the complex coastline or near the islands. MODIS and OSTIA SST also have the same problem because of the coarse spatial resolution of 1 km and 0.05° , respectively [47]. In this context, the outlier removal can be essential for the QC of all SST products.

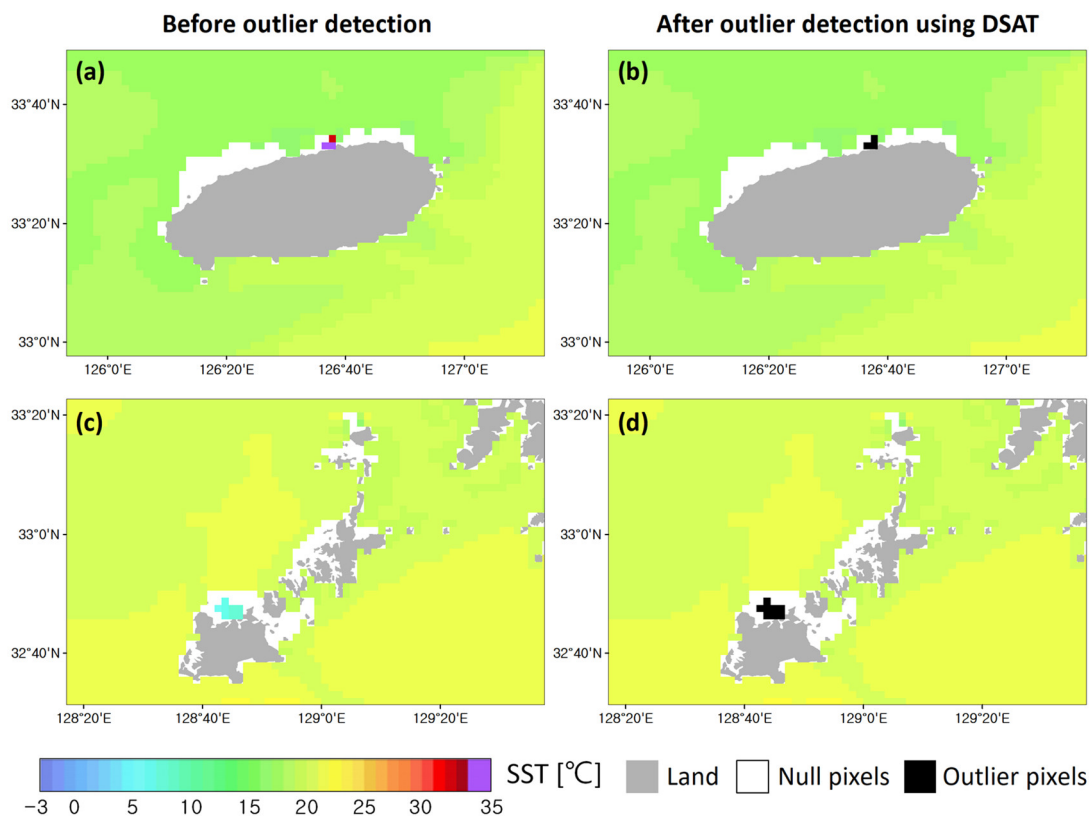


Figure 11. GK2A SST maps before and after outlier detection on 1 June 2020. (a,b): The mean SST of the three outlier pixels is $36.01\text{ }^{\circ}\text{C}$, whereas the mean SST of the other pixels ($n = 322$) is $17.18\text{ }^{\circ}\text{C}$. (c,d): The mean SST of the eight outlier pixels is $6.72\text{ }^{\circ}\text{C}$, whereas the mean SST of the other pixels ($n = 541$) is $20.54\text{ }^{\circ}\text{C}$.

5.2. Gap-Filling Accuracy Using MLR and RRK

The MLR model for the spatial gap-filling of GK2A daily SST around Korean Peninsula was built, as shown in Equation (8):

$$GK2A = \beta_0 + \beta_{clim}Clim + \beta_{SH}SH + \beta_{WMS}WMS + \varepsilon \quad (8)$$

where the target variable $GK2A$ denotes GK2A SST, and the explanatory variables $Clim$, SH , and WMS indicate the OSTIA daily SST climatology value, LDAPS specific humidity, and LDAPS maximum wind speed, respectively. β_{clim} , β_{SH} , and β_{WMS} are regression coefficients corresponding to each explanatory variable. β_0 is the intercept and ε is the error term. The regression coefficients were all significant with $p < 0.01$. The coefficient of determination (R^2) was 0.965, indicating that the meteorological factors can explain the GK2A SST variation very appropriately (Table 5).

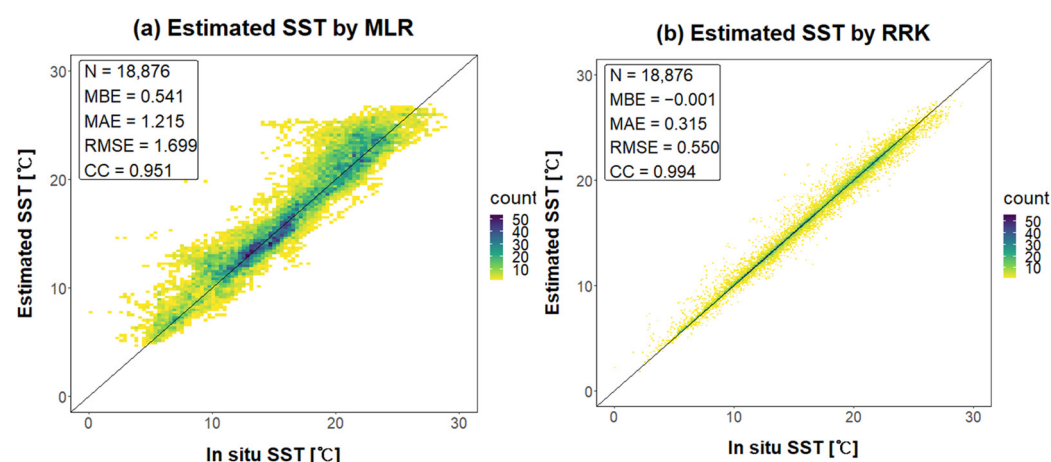
Table 5. Summary of the MLR model for the pixels where GK2A SST and the in situ SST measurements existed in 2020.

Explanatory Variables	β Coefficient	p -Value	R^2	N
Constant	2.525	<0.01	0.965	27,099
OSTIA daily SST climatology	0.824	<0.01		
LDAPS specific humidity	62.459	<0.01		
LDAPS maximum wind speed	−0.024	<0.01		

The MLR estimates were derived for gap-filling of the 18,876 pixels where GK2A had null values, and the in situ SST measurements existed. The accuracy statistics were calculated for the gap-filled 18,876 pixels (Figure 12). The MLR gap-filling showed the MBE of 0.541 °C, RMSE of 1.699 °C, and the CC of 0.951 before applying the RRK. Then, the RRK was applied to the same 18,876 pixels and produced the MBE of −0.001 °C, RMSE of 0.550 °C, and the CC of 0.994, which was a much improved result by the residual compensation. Additional accuracy statistics were calculated for the whole pixels, including the original and the gap-filled pixels on the 45,975 in situ measurement points (Figure 13). The MLR modeling had the MBE = 0.341 °C, RMSE = 1.341 °C, and CC = 0.970, and the RRK modeling produced the MBE = 0.119 °C, RMSE = 0.858 °C, and CC = 0.987 (Table 6). It is remarkable that the RRK gap-filling showed higher accuracy (CC = 0.994) than the original GK2A data.

Table 6. Accuracy statistics of GK2A SST estimate by MLR and RRK.

	Type	N	MBE	MAE	RMSE	CC
MLR	Gap-filling estimates	18,876	0.541	1.215	1.699	0.951
	Both original data and gap-filling estimates	45,975	0.341	0.896	1.341	0.970
RRK	Gap-filling estimates	18,876	−0.001	0.315	0.550	0.994
	Both original data and gap-filling estimates	45,975	0.119	0.526	0.858	0.987

**Figure 12.** Scatter plots for the in situ SST and estimated SST by (a) MLR, and (b) RRK. The number of validation (N = 18,876) is for the pixels where GK2A had null values, and the in situ measurements existed in 2020.

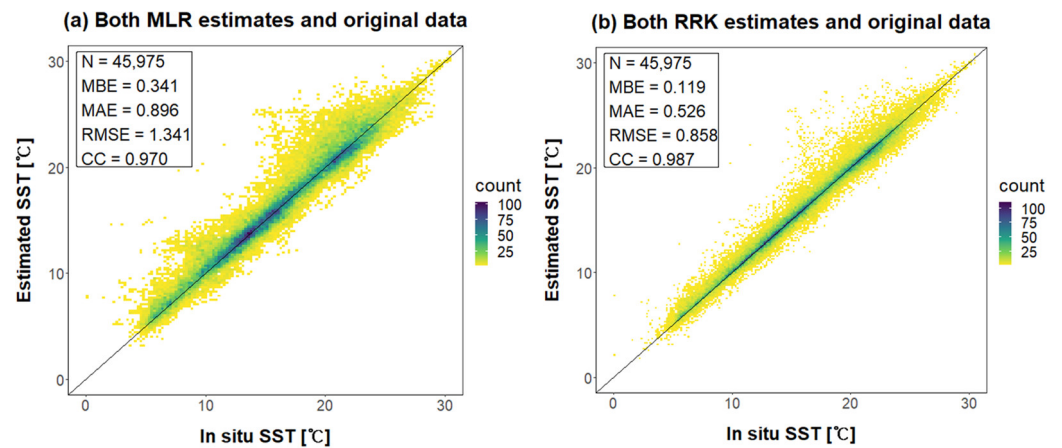


Figure 13. Scatter plots for the whole in situ measurement points ($N = 45,975$). (a) including both MLR estimates and original data, and (b) including both RRK estimates and original data.

Figure 14 shows the GK2A SST maps before and after applying MLR and RRK modeling with the example of 18 March, 31 August, and 3 November, 2020. In both maps, the overall gap-filling results look similar. However, the MLR gap-filling had more significant differences (from 1.0 to 2.0 °C lower) from the neighboring pixels, showing a bit of discontinuity around the border of the gap-filled pixels (35°N and 130°E on 31 August 2020). On the other hand, the RRK presented a more natural and continuous spatial pattern around the gap-filled pixels with fewer differences from the neighboring pixels. In Figure 15, the Tongyeong station on 20 July 2020, had an in situ SST of 21.30 °C, and the MLR and RRK estimates were 23.41 °C and 21.28 °C, respectively. The MLR gap-filling was about 2 °C overestimated, whereas the RRK result was almost the same as the in situ SST. The distribution of estimates around the Tongyeong station was also more reasonable in the RRK model results reflecting the residual trend with the surrounding in situ SST.

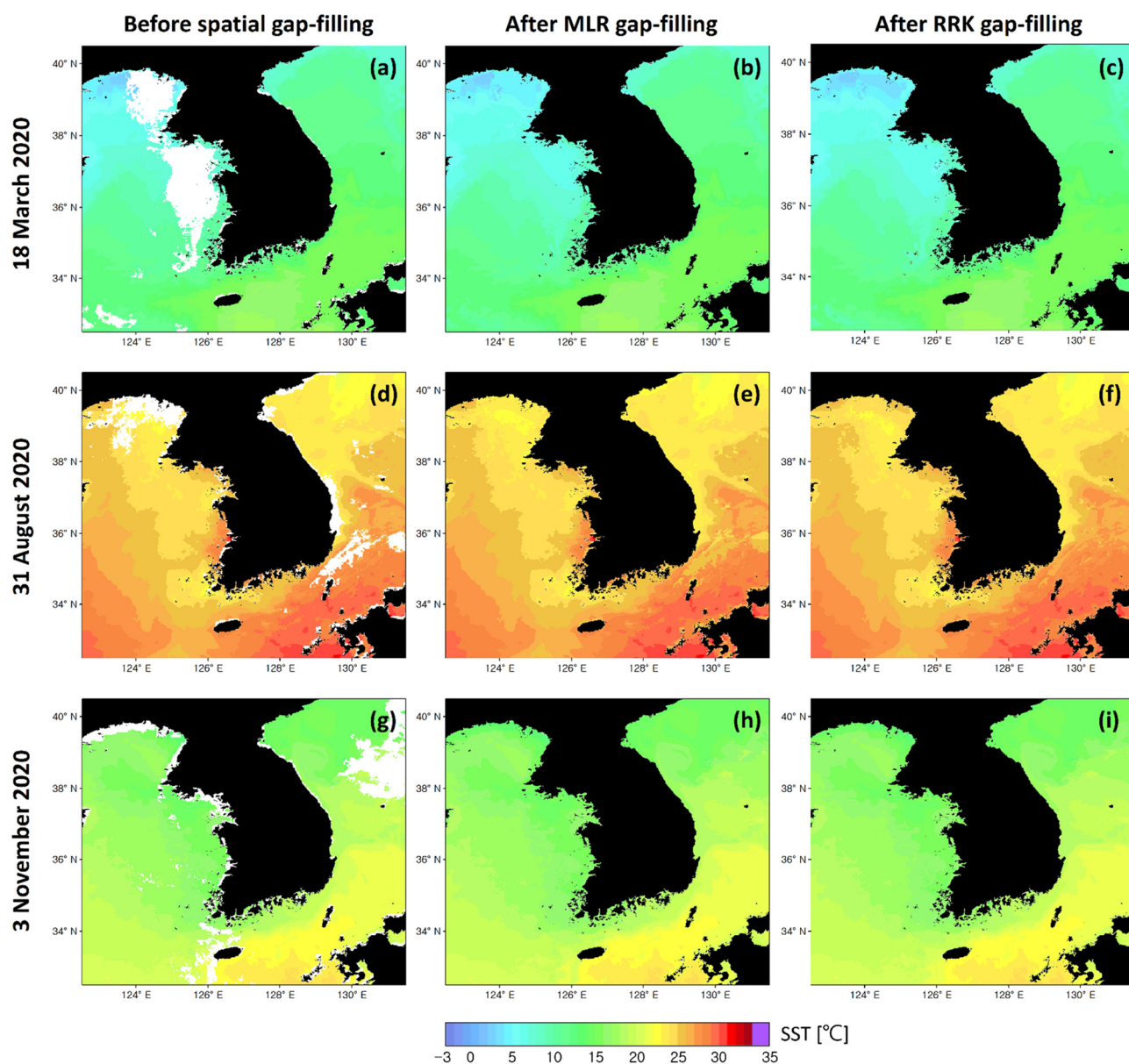


Figure 14. GK2A SST maps before and after the MLR and RRK gap-filling with the example of 18 March, 31 August, and 3 November, 2020. (a,d,g) denote images before spatial gap-filling. (b,e,h) gap-free SST after MLR, and (c,f,i) gap-free SST after RRK.

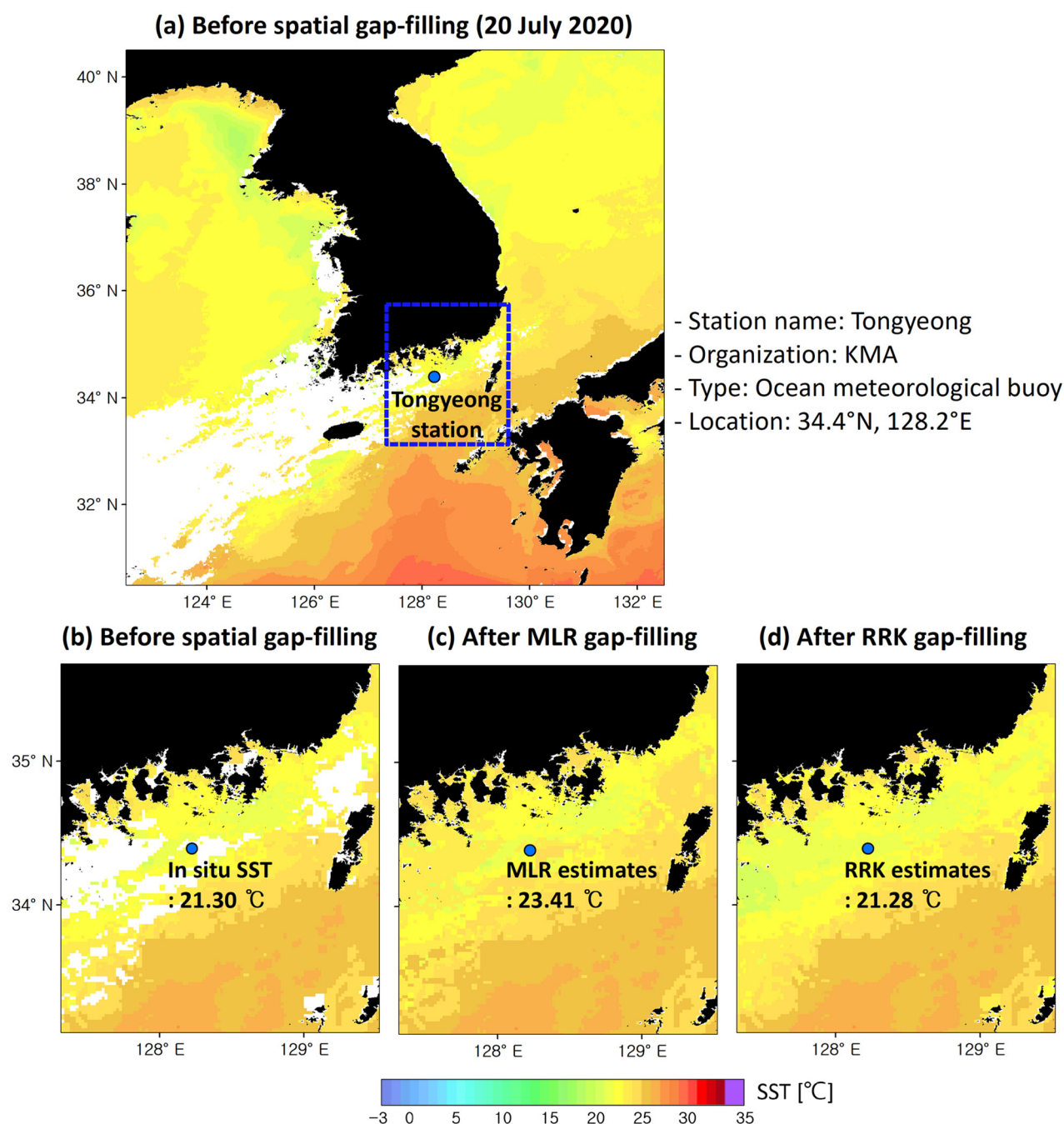


Figure 15. GK2A SST maps before and after the MLR and RRK gap-filling around the Tongyeong station on 20 July 2020. **(a)** The location of the Tongyeong station in the study area. **(b)** denote images before spatial gap-filling. **(c)** gap-free SST after MLR, and **(d)** gap-free SST after RRK. The RRK showed a more reasonable result similar to the in situ measurement.

5.3. Gap-Filling Accuracy for the Far Seas

The null pixel ratio of the GK2A daily SST in 2020 is summarized in Table 7. We conducted another accuracy test for the in situ measurements in the far seas using the daily SST images with a null pixel ratio of less than 0.4 because most images (72.68%) had a null pixel ratio of less than 0.4. Nine stations (Ongjinsocheongcho, Incheon, Seohae 170, Seohae 206, Sinangageocho, Ulsan, Pohang, Uljin, and Donghae) that are more than 30 km away from the coastline were selected as the validation reference (Figure 1c). Table 8 shows the accuracy statistics of the MLR gap-filling (MBE = 0.285 °C, RMSE = 1.581 °C,

and $CC = 0.964$) and RRK gap-filling ($MBE = -0.094$ °C, $RMSE = 0.401$ °C, and $CC = 0.997$), respectively. The accuracy of RRK was very high in the far seas, showing a concentrated scatter plot on the 1:1 line (Figure 16). Figure 17 shows the GK2A SST maps before and after gap-filling around the Incheon station on 17 March 2020. The in situ measurement was 6.09 °C, and the MLR and RRK estimates were 6.54 °C and 6.18 °C, respectively. The RRK gap-filling rarely showed under- or over-estimation tendencies in both near and far seas, indicating that the residual compensation was adequate to supplement the MLR modeling.

Table 7. Null pixel ratio of GK2A daily SST in 2020.

Null Pixel Ratio	Number of Images	Percentage
0.0 to 0.1	117	31.97
0.1 to 0.2	67	18.31
0.2 to 0.3	51	13.93
0.3 to 0.4	31	8.47
0.4 to 0.5	41	11.20
0.5 to 0.6	18	4.92
0.6 to 0.7	18	4.92
0.7 to 0.8	18	4.92
0.8 to 0.9	5	1.37
0.9 to 1.0	0	0
Total	366	100

Table 8. Accuracy statistics of the MLR and RRK gap-filling using the GK2A SST images with the null pixel ratio less than 0.4 in the far seas (outside 30 km buffer).

Type	N	MBE	MAE	RMSE	CC
MLR	252	0.285	1.225	1.581	0.964
RRK	252	−0.094	0.229	0.401	0.997

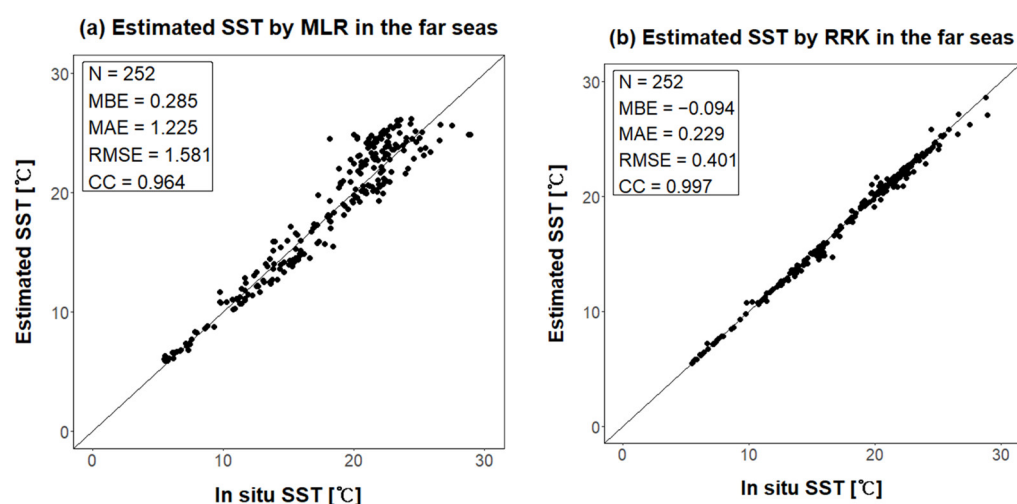


Figure 16. Scatter plots of the (a) MLR and (b) RRK gap-filling using the GK2A SST images with the null pixel ratio less than 0.4 in the far seas (outside 30 km buffer).

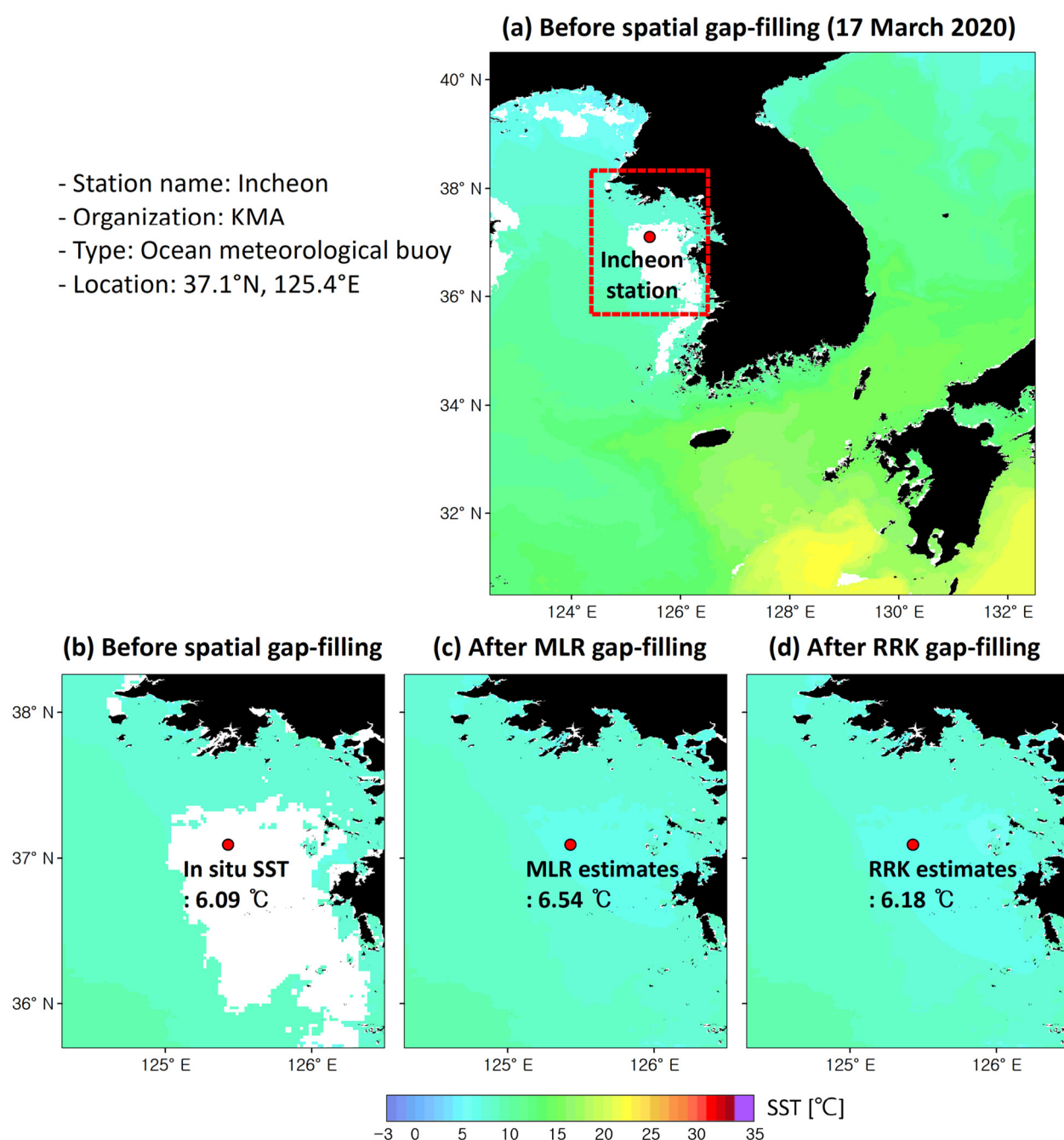


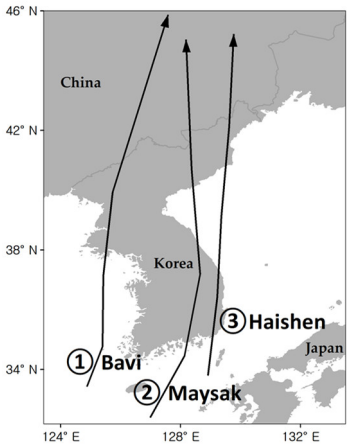
Figure 17. GK2A SST maps before and after the MLR and RRK gap-filling around the Incheon station on 17 March 2020. (a) The location of the Incheon station in the study area. (b) denote images before spatial gap-filling. (c) gap-free SST after MLR, and (d) gap-free SST after RRK.

5.4. Influence of Typhoons

A typhoon is an extreme meteorological event that can cause an abrupt change in SST. Table 9 shows the typhoons that affected the Korean Peninsula between August and September 2020 [48]. Maysak and Haishen passed through the East Sea from the end of August to the beginning of September. Strong winds in the typhoons caused an upwelling and vertical mixing of seawater, which resulted in a decrease in SST [49,50]. In situ SST at Donghae station sharply decreased about 4–5 °C from 26.13 °C on 2 September to 21.52 °C on 3 September due to the typhoons. The SST was continued with an average of 20 to 21 °C for the time being (Figure 18). Figure 19 shows the GK2A SST maps before and after

the MLR and RRK gap-filling for Donghae station on 4 September 2020. The in situ SST was 21.43 °C, and the MLR estimate was 22.93 °C showing a 1.50 °C overestimation. This may be the limitation of linear modeling and the need for nonlinear modeling such as machine learning and neural networks. Change detection algorithms such as jumps upon spectrum and trend (JUST) [51], breaks for additive season and trend (BFAST) [52], and continuous change detection and classification (CCDC) [53] may be utilized for abrupt change detections and better trend estimations. On the other hand, the RRK model showed a better estimate of 21.38 °C with only a 0.05 °C difference from the in situ measurement. If nonlinear regression models based on artificial intelligence techniques are combined with the RRK method, it can appropriately handle unexpected cases such as extreme weather events.

Table 9. Information on typhoons that affected the Korean Peninsula from August to September 2020.

Track of typhoon	No.	Name	Formation and Extinction (UTC)
	1	Bavi	22 August 2020 00:00~27 August 2020 06:00
	2	Maysak	28 August 2020 06:00~3 September 2020 03:00
	3	Haishen	1 September 2020 12:00~7 September 2020 12:00

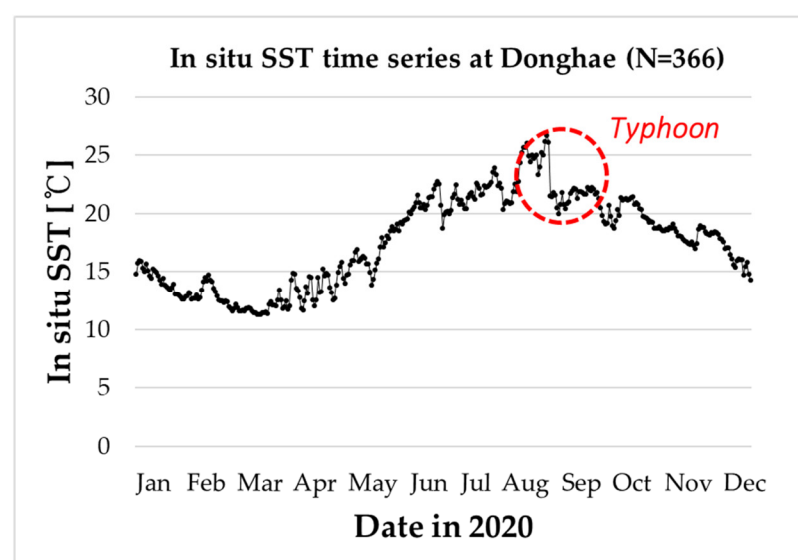


Figure 18. The in situ SST measurements at Donghae in 2020. A sharp decrease from 26.13 °C to 21.52 °C occurred due to typhoons.

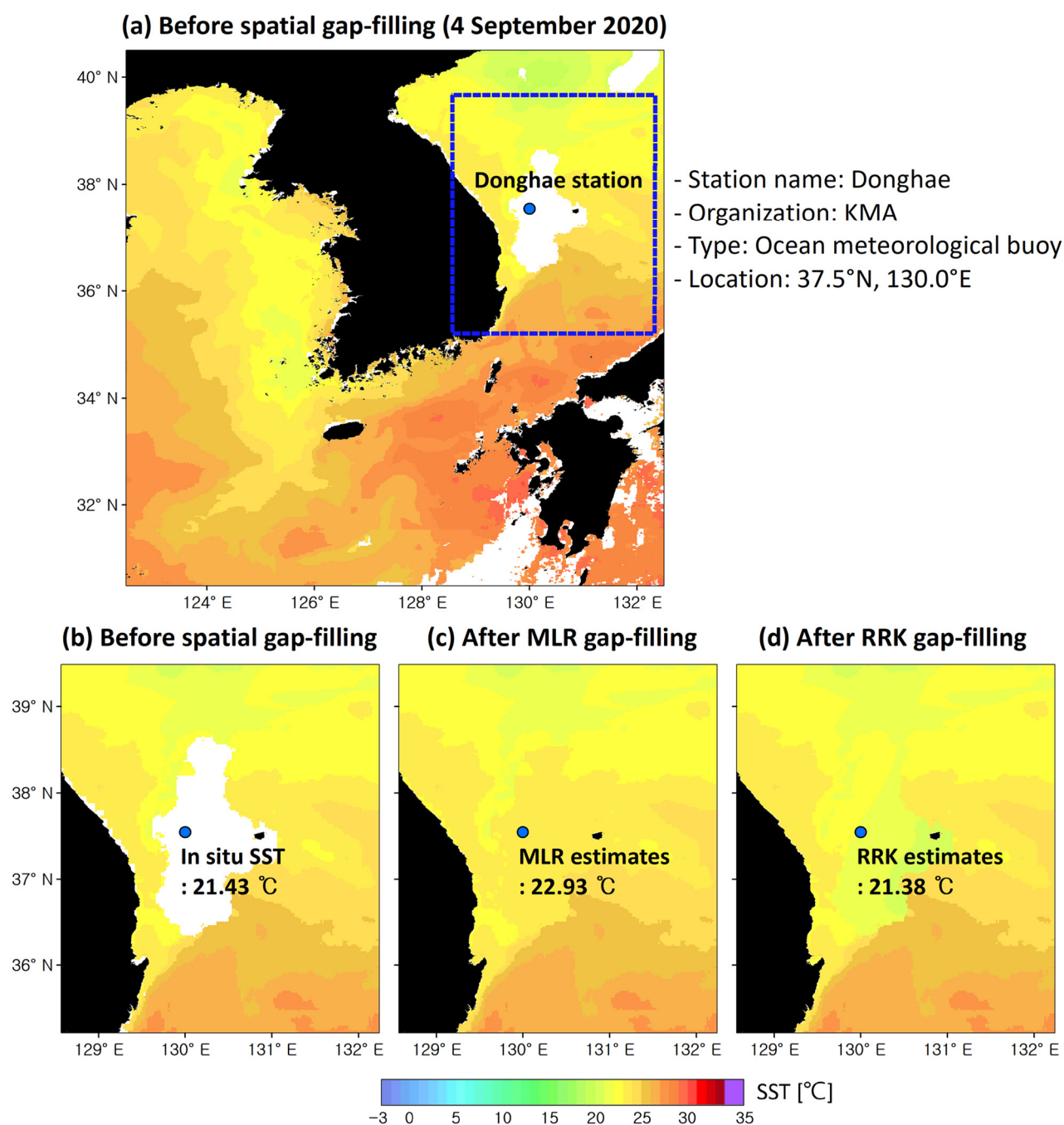


Figure 19. GK2A SST maps before and after the MLR and RRK gap-filling around the Donghae station on 4 September 2020. **(a)** The location of the Donghae station in the study area. **(b)** denote images before spatial gap-filling. **(c)** gap-free SST after MLR, and **(d)** gap-free SST after RRK. The RRK result was stable under the influence of typhoons because it can cope with the abrupt changes in marine meteorology.

6. Conclusions

In this paper, a spatial gap-filling of GK2A daily SST in 2020 was conducted using RRK for the seas around the Korean Peninsula. Extreme outliers were first removed from the in situ measurements and from the GK2A daily SST images using multi-step statistical procedures. For the pixels on the in situ measurements after the quality control, an MLR model was built using the selected meteorological variables such as daily SST climatology value, specific humidity, and maximum wind speed. The irregular point residuals from

the MLR model were transformed to a residual grid by an optimized kriging for the residual compensation for the MLR estimation of the null pixels. The RRK residual compensation method produced greatly improved accuracy compared with the in situ measurements. The gap-filled 18,876 pixels showed the MBE of -0.001 °C, the MAE of 0.315 °C, the RMSE of 0.550 °C, and the CC of 0.994 . The case studies made sure that the gap-filled SST with RRK had very similar values to the in situ measurements than those of the MLR-only method. In terms of RMSE, the RRK result was 68% improved than the MLR-only $(1.69-0.550)/1.699$. This was more apparent in the typhoon case: our RRK result was also stable under the influence of typhoons because it can cope with the abrupt changes in marine meteorology. An essential implication of this study is that the proposed method can be used as an operational framework for the gap-free GK2A daily SST product. In terms of time dimension, we used just one image for gap-filling. The gap-filling value was derived from multiple meteorological variables at the same time. Considering the temporal correlation of SST, multiple temporal images can be also used in a future work.

Author Contributions: Conceptualization, J.A. and Y.L.; methodology, J.A. and Y.L.; data curation, J.A.; writing—original draft preparation, J.A. and Y.L.; writing—review and editing, J.A. and Y.L.; All authors have read and agreed to the published version of the manuscript.

Funding: This research received no external funding.

Acknowledgments: This research was supported by the “Monitoring System of Spilled Oils Using Multiple Remote Sensing Techniques” funded by the Korea Coast Guard, Korea.

Conflicts of Interest: The authors declare no conflict of interest.

References

1. Yan, Y.; Barth, A.; Beckers, J.-M.; Candille, G.; Brankart, J.-M.; Brasseur, P. Ensemble assimilation of ARGO temperature profile, sea surface temperature, and altimetric satellite data into an eddy permitting primitive equation model of the North Atlantic Ocean. *J. Geophys. Res. Ocean* **2015**, *120*, 5134–5157.
2. Dai, A. Future warming patterns linked to today’s climate variability. *Sci. Rep.* **2016**, *6*, 19110.
3. Donlon, C.; Robinson, I.; Casey, K.S.; Vazquez-Cuervo, J.; Armstrong, E.; Arino, O.; Gentemann, C.; May, D.; LeBorgne, P.; Piollé, J.; et al. The global ocean data assimilation experiment high-resolution sea surface temperature pilot project. *Bull. Am. Meteorol. Soc.* **2007**, *88*, 1197–1213.
4. Maturi, E.; Harris, A.; Mittaz, J.; Sapper, J.; Wick, G.; Zhu, X.; Dash, P.; Koner, P. A new high-resolution sea surface temperature blended analysis. *Bull. Am. Meteorol. Soc.* **2017**, *98*, 1015–1026.
5. Tu, Q.; Hao, Z. Validation of sea surface temperature derived from Himawari-8 by JAXA. *IEEE J. Sel. Top. Appl. Earth Obs. Remote Sens.* **2020**, *13*, 448–459.
6. Jones, M.S.; Saunders, M.A.; Guymer, T.H. Reducing cloud contamination in ATSR averaged sea surface temperature data. *J. Atmos. Ocean Technol.* **1996**, *13*, 492–506.
7. May, D.A.; Stowe, L.L.; Hawkins, J.D.; McClain, E.P. A correction for Saharan dust effects on satellite sea surface temperature measurements. *J. Geophys. Res. Ocean* **1992**, *97*, 3611–3619.
8. Al-Shehhi, M.R. Uncertainty in satellite sea surface temperature with respect to air temperature, dust level, wind speed and solar position. *Reg. Stud. Mar. Sci.* **2022**, *53*, 102385.
9. Azad, M.T.; Lari, K.; Oudi, R.; Sadeghifar, T.; Kisi, O. The effect of dust storm on sea surface temperature in the Western Basin of Persian Gulf. *Standards* **2022**, *2*, 246–259.
10. Gohin, F.; Langlois, G. Using geostatistics to merge in situ measurements and remotely-sensed observations of sea surface temperature. *Int. J. Remote Sens.* **1993**, *14*, 9–19.
11. Zhu, Y.; Kang, E.L.; Bo, Y.; Tang, Q.; Cheng, J.; He, Y. A Robust Fixed Rank Kriging method for improving the spatial completeness and accuracy of satellite SST Products. *IEEE Trans. Geosci. Remote Sens.* **2015**, *53*, 5021–5035.
12. Alvera-Azcárate, A.; Barth, A.; Rixen, M.; Beckers, J.M. Reconstruction of incomplete oceanographic data sets using empirical orthogonal functions: Application to the Adriatic Sea surface temperature. *Ocean Model.* **2005**, *9*, 325–346.
13. Alvera-Azcárate, A.; Barth, A.; Beckers, J.-M.; Weisberg, R.H. Multivariate reconstruction of missing data in sea surface temperature, chlorophyll, and wind satellite fields. *J. Geophys. Res.* **2007**, *112*, C03008. <https://doi.org/10.1029/2006JC003660>.
14. Beckers, J.M.; Rixen, M. EOF calculations and data filling from incomplete oceanographic datasets. *J. Atmos. Ocean. Technol.* **2003**, *20*, 1839–1856.
15. Youzhuan, D.; Dongyang, F.; Zhihui, W.; Zhihua, M.; Juhong, Z. Reconstruction of incomplete satellite oceanographic data sets based on EOF and Kriging methods. In Proceedings of the Image and Signal Processing for Remote Sensing XIV. SPIE, Cardiff, Wales, UK, 10 October 2008; Volume 7109.

16. Nellikkattil, A.B. Filling of Gaps in Sea Surface Temperature Using Artificial Neural Network. Master's Thesis, University of Hyderabad, Hyderabad, India, 2016. <https://doi.org/10.13140/RG.2.2.33600.64004>.
17. Bolat, F.; Bulut, S.; Günlü, A.; Ercanlı, İ.; Şenyurt, M. Regression kriging to improve basal area and growing stock volume estimation based on remotely sensed data, terrain indices and forest inventory of black pine forests. *N. Z. J. For. Sci.* **2020**, *50*, 1–11.
18. Hengl, T.; Heuvelink, G.B.M.; Rossiter, D.G. About regression-kriging: From equations to case studies. *Comput. Geosci.* **2007**, *33*, 1301–1315.
19. Kang, E.; Yoo, C.; Shin, Y.; Cho, D.; Im, J. Comparative Assessment of Linear Regression and Machine Learning for Analyzing the Spatial Distribution of Ground-level NO₂ Concentrations: A Case Study for Seoul, Korea. *Korean J. Remote Sens.* **2021**, *37*, 1739–1756. (In Korean with English abstract)
20. Kim, J.; Lee, J. Analysis of the spatial distribution of total phosphorus in wetland soils using geostatistics. *J. Korean Soc. Environ. Eng.* **2016**, *38*, 551–557. (In Korean with English abstract)
21. Llamas, R.M.; Guevara, M.; Rorabaugh, D.; Taufer, M.; Vargas, R. Spatial Gap-Filling of ESA CCI Satellite-Derived Soil Moisture Based on Geostatistical Techniques and Multiple Regression. *Remote Sens.* **2020**, *12*, 665.
22. Odeh, I.O.A.; McBratney, A.B.; Chittleborough, D.J. Further results on prediction of soil properties from terrain attributes: Heterotopic cokriging and regression-kriging. *Geoderma* **1995**, *67*, 215–226.
23. Park, H.; Shin, H.; Roh, Y.; Kim, K.; Park, K. Estimating forest carbon stocks in Danyang using kriging methods for aboveground biomass. *J. Korean Assoc. Geogr. Inf. Stud.* **2012**, *15*, 16–33. (in Korean with English abstract)
24. Gia Pham, T.; Kappas, M.; Van Huynh, C.; Hoang Khanh Nguyen, L. Application of Ordinary Kriging and Regression Kriging Method for Soil Properties Mapping in Hilly Region of Central Vietnam. *Int. J. Geo-Inf.* **2019**, *8*, 147.
25. Kim, M.; Heo, J.; Sohn, E. Atmospheric correction of true-color RGB imagery with Limb Area-Blending based on 6S and satellite image enhancement techniques using Geo-Kompsat-2A Advanced Meteorological Imager data. *Asia-Pac. J. Atmos. Sci.* **2021**, *58*, 333–352.
26. Kim, D.; Gu, M.; Oh, T.-H.; Kim, E.-K.; Yang, H.-J. Introduction of the Advanced Meteorological Imager of Geo-Kompsat-2a: In-orbit tests and performance validation. *Remote Sens.* **2021**, *13*, 1303.
27. NMSC (National Meteorological Satellite Center). Web-Based Data Service of the GK2A and COMS. 2022. <https://datasvc.nmsc.kma.go.kr> (accessed on 31 August 2022).
28. NMSC (National Meteorological Satellite Center). GK2A AMI Algorithm Theoretical Basis Document. 2019. <https://nmsc.kma.go.kr/homepage/html/base/cmm/selectPage.do?page=static.edu.atbdGk2a> (accessed on 31 August 2022).
29. Kramar, M.; Ignatov, A.; Petrenko, B.; Kihai, Y.; Dash, P. Near real time SST retrievals from Himawari-8 at NOAA using ACSPO system. In Proceedings of the Ocean Sensing and Monitoring VIII, Baltimore, MD, USA, 17 April 2016; p. 98270.
30. Shin, Y.; Yi, C. Statistical downscaling of urban-scale air temperatures using an analog model output statistics technique. *Atmosphere* **2019**, *10*, 427.
31. Kim, D.; Kang, G.; Kim, D.; Kim, J. Characteristics of LDAPS-predicted surface wind speed and temperature at automated weather stations with different surrounding land cover and topography in Korea. *Atmosphere* **2020**, *11*, 1224.
32. Good, S.; Fiedler, E.; Mao, C.; Martin, M.J.; Maycock, A.; Reid, R.; Roberts-Jones, J.; Searle, T.; Waters, J.; While, J.; Worsfold, M. The current configuration of the OSTIA system for operational production of foundation sea surface temperature and ice concentration analyses. *Remote Sens.* **2020**, *12*, 720.
33. KMA (Korea Meteorological Administration). *May 2013 Weather Information for Coastal Ships*; Korea Meteorological Administration: Seoul, Korea, 2013. https://www.kma.go.kr/marine/marine_08/pdf/data_201305.pdf (accessed on 31 August 2022).
34. KMA (Korea Meteorological Administration). *Coastal Wave Buoy*; KMA Weather Data Service: Seoul, Korea, 2022. <https://data.kma.go.kr/data/sea/selectFargoBuoyRltmList.do?pgmNo=55> (accessed on 31 August 2022).
35. Xie, J.; Zhu, J.; Li, Y. Assessment and inter-comparison of five high-resolution sea surface temperature products in the shelf and coastal seas around China. *Cont. Shelf Res.* **2008**, *28*, 1286–1293.
36. Baek, Y.; Moon, I. The accuracy of satellite-composite GHRSSST and model-reanalysis sea surface temperature data at the seas adjacent to the Korean Peninsula. *Ocean Polar Res.* **2019**, *41*, 213–232. (In Korean with English abstract)
37. Woo, H.; Park, K.; Choi, D.; Byun, D.; Jeong, K.; Lee, E. Comparison of multi-satellite sea surface temperatures and in-situ temperatures from Jeodo ocean research station. *J. Korean Earth Sci. Soc.* **2019**, *40*, 613–623. (In Korean with English abstract)
38. U.S. Integrated Ocean Observing System (U.S. IOOS). *Manual for Real-Time Quality Control of In-Situ Temperature and Salinity Data Version 2.1: A Guide to Quality Control and Quality Assurance of In-Situ Temperature and Salinity Observations*; U.S. Department of Commerce, National Oceanic and Atmospheric Administration, National Ocean Service, Integrated Ocean Observing System: Silver Spring, MD, USA, 2020; 50p.
39. Alvera-Azcárate, A.; Sirjacobs, D.; Barth, A.; Beckers, J.-M. Outlier detection in satellite data using spatial coherence. *Remote Sens. Environ.* **2012**, *119*, 84–91.
40. Hawkins, S.; He, H.; Williams, G.; Baxter, R. Outlier detection using Replicator Neural Networks. In Proceedings of the International Conference on Data Warehousing and Knowledge Discovery, Aix-en-Provence, France, 4–6 September, 2002; pp. 170–180.
41. Kern, M.; Preimesberger, T.; Allesch, M.; Pail, R.; Bouman, J.; Koop, R. Outlier detection algorithms and their performance in GOCE gravity field processing. *J. Geod.* **2005**, *78*, 509–519.

42. Ahn, J.; Lee, Y. Outlier detection and gap-filling of the GK2A daily Sea Surface Temperature (SST) product using statistical methods. *J. Clim. Res.* **2021**, *16*, 327–346. (In Korean with English abstract)
43. Anselin, L.; Bera, A.K. *Spatial Dependence in Linear Regression Models with an Introduction to Spatial Econometrics*; Handbook of Applied Economic Statistics: New York, NY, USA, 1998; pp. 237–289.
44. Anselin, L. The Moran Scatterplot as an ESDA Tool to Assess Local Instability in Spatial Association. In *Spatial Analytical Perspectives on GIS*; Taylor and Francis: London, UK, 1996; pp. 111–125.
45. Cressie, N. Fitting variogram models by weighted least squares. *J. Int. Assoc. Math. Geol.* **1985**, *17*, 563–586.
46. Ahn, J.; Lee, Y. Ordinary Kriging of daily mean SST (Sea Surface Temperature) around South Korea and the analysis of interpolation accuracy. *J. Korean Soc. Surv. Geod. Photogramm. Cartogr.* **2022**, *40*, 51–66. (in Korean with English abstract)
47. Kang, K.; Kim, D.; Kim, S.; Cho, Y.; Lee, S. Extraction of sea surface temperature in coastal area using ground-based thermal infrared sensor on-boarded to aircraft. *Korean J. Remote Sens.* **2014**, *30*, 797–807. (in Korean with English abstract)
48. Ha, K. Short communication: Predicting typhoon tracks around Korea. *Nat. Hazards* **2022**, *113*, 1385–1390. <https://doi.org/10.1007/s11069-022-05335-6>.
49. Subrahmanyam, M.V.; Shengyan, Y.; Raju, P.V.S. Typhoon Haikui induced sea surface temperature cooling and rainfall influence over Zhejiang coastal waters. *Atmósfera* **2021**, *34*, 385–394.
50. Sun, L.; Yang, Y.; Xian, T.; Lu, Z.; Fu, Y. Strong enhancement of chlorophyll *a* concentration by a weak typhoon. *Mar. Ecol. Prog. Ser.* **2010**, *404*, 39–50.
51. Ghaderpour, E.; Vujadinovic, T. Change detection within remotely sensed satellite image time series via spectral analysis. *Remote Sens.* **2020**, *12*, 4001. <https://doi.org/10.3390/rs12234001>.
52. Masiliūnas, D.; Tsendbazar, N.; Herold, M.; Verbesselt, J. BFAST Lite: A lightweight break detection method for time series analysis. *Remote Sens.* **2021**, *13*, 3308. <https://doi.org/10.3390/rs13163308>.
53. Awty-Carroll, K.; Bunting, P.; Hardy, A.; Bell, G. Using continuous change detection and classification of Landsat data to investigate long-term mangrove dynamics in the Sundarbans region. *Remote Sens.* **2019**, *11*, 2833. <https://doi.org/10.3390/rs11232833>.